Fuel Cells Bulletin
ISSN: 1464-2859

The Suppression of Thrust Ripple and Electromagnetic Vibration in A Double-sided Flux Switching Permanent Magnet Linear Motor by Optimizing the Stator Structure

Wei Du[1]*, Haonan Cui[1], Cheng Wen[1], Zengqiang Ma[1]

1. School of Electrical and Electronic Engineering, Shijiazhuang Tiedao University, Shijiazhuang, China
Corresponding Author's Email: duwei571@126.com

Abstract: The Double-Sided Flux Switching Permanent Magnet Linear Motor (DLFSPM) is being increasingly and extensively employed in various fields due to its merits of high efficiency and high power density. Nevertheless, the DLFSPM suffer from significant thrust ripple, which exacerbates electromagnetic vibration. To effectively reduce thrust ripple and electromagnetic vibration, this paper aims to significantly enhance its performance by optimizing the stator structure. Firstly, establish the finite element analysis model of the DLFSPM, and based on theoretical methods, derive the electromagnetic thrust equation and the equation of electromagnetic vibration, clarifying the key indicators. Secondly, effective suppression of thrust ripple is achieved by optimizing the radius of the arc fillet in the stator slot. Subsequently, auxiliary slots are introduced on the stator tooth surface, and their optimal dimensions are determined using the finite element model and response surface methodology, with the objective functions of enhancing electromagnetic thrust and reducing thrust ripple. Finally, a comparative analysis is conducted between the comprehensively optimized DLFSPM and the initial structure motor regarding electromagnetic thrust, thrust ripple, and electromagnetic vibration. The simulation results demonstrate that the optimized DLFSPM not only significantly improves electromagnetic thrust but also effectively suppresses thrust ripple and electromagnetic vibration, thereby validating the effectiveness of the optimization method.

Keywords: DLFSPM; thrust ripple; Electromagnetic Vibration; Stator structure optimization; finite element analysis

1. Introduction

In the wake of the advancement of industrial technology, the superiority of the double-sided flux-switching permanent magnet linear motor (DLFSPM) in pertinent domains such as the feed system of precision machine tools, electromagnetic propulsion, and rail transportation has manifested itself with escalating prominence[1,2]. By virtue of its unique bilateral flux-switching technology, the DLFSPM optimize the magnetic flux path, significantly enhancing thrust density and efficiency while effectively reducing the motor's size and weight.

However, due to the distinctive double salient pole structure of the DLFSPM and its magnetic pole merging effect, this motor exhibits a higher flux density. Consequently, magnetic saturation is likely to occur in specific primary and secondary teeth [3], resulting in significant pulsation of the output electromagnetic thrust and inducing mechanical vibrations and noise[4,5]. These phenomena ultimately compromise the operational efficiency and stability of the motor. Research on DLFSPM has attracted extensive attention from many scholars[6,7], particularly since Cheng et al. proposed the air-gap magnetic field modulation theory[8]. Drawing on this theoretical framework, a considerable body of research has emerged regarding flux-switching motors[9,10,11]. However, the majority of existing studies have concentrated on the principles of thrust generation, motor efficiency, and improvements in thrust performance [12], while comparatively limited attention has been paid to the analysis of thrust ripple phenomena in DLFSPM. To mitigate thrust fluctuations, and suppress electromagnetic vibrations, it is imperative to optimize the stator structure of the DLFSPM.

In this paper, the stator structure of the DLFSPM is optimized, and a two-dimensional finite element model is established for analysis in order to alleviate thrust ripple and suppress electromagnetic vibration. Firstly, the stator slot structure is optimized to determine the optimal arc chamfer radius. Subsequently, the stator tooth structure is enhanced by introducing auxiliary slots, aiming to reduce electromagnetic thrust ripple and electromagnetic noise. Finally, a comprehensive comparative analysis of the electromagnetic performance between the optimized motor and the initial structure is conducted to validate the effectiveness of the proposed optimization scheme.

2. The initial structure and electromagnetic performance of DLFSPM

2.1 The initial structure of DLFSPM

The fundamental configuration of the DLFSPM, as depicted in Figure 1, consists of two symmetrical elongated secondary stators and a single compact primary mover. During the operation of DLFSPM, the mover is actuated by the interaction between the armature magnetic field and the permanent magnet field, leading to a design that is both structurally simple and capable of generating substantial electromagnetic thrust. The initial structural dimensions and parameters of the DLFSPM are shown in Table 1.

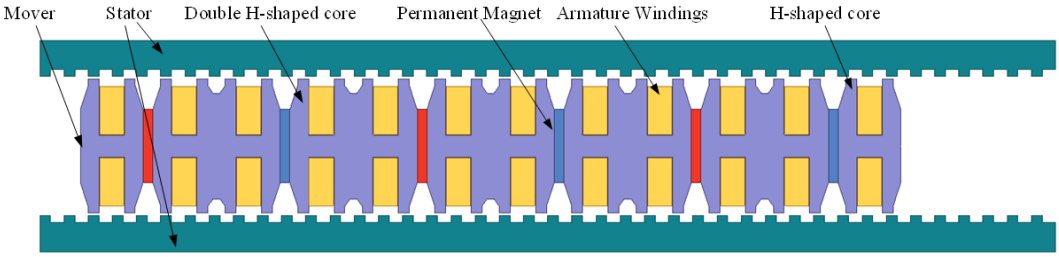

Figure. 1 The initial structure of DLFSPM.

Table 1 Parameters of the DLFSPM

Items	Specifications	Items	Specifications
Air gap g/mm	1	Permanent magnet thickness /mm	4
Secondary pole pitch /mm	9.9	Permanent magnet height/mm	30
Secondary tooth width /mm	4.455	Motor longitudinal depth/mm	150
Secondary tooth height/mm	2.8	Primary tooth pitch /mm	14.85
Secondary yoke height/mm	12	Primary tooth width/mm	4.455

2.2 Electromagnetic properties based on the initial structure of DLFSPM

Finite element analysis (FEA), a widely accepted methodology for motor modeling, enables the optimization of motor design through the simulation of electromagnetic properties. In contrast to rotary motors, linear motors feature an extended air gap and a larger intersection area between air gap and the mover's travel range. To enhance the accuracy of the finite element model for the DLFSPM, a four-layer meshing scheme for the air-gap magnetic field has been employed. The resulting mesh division is depicted in Figure 2.

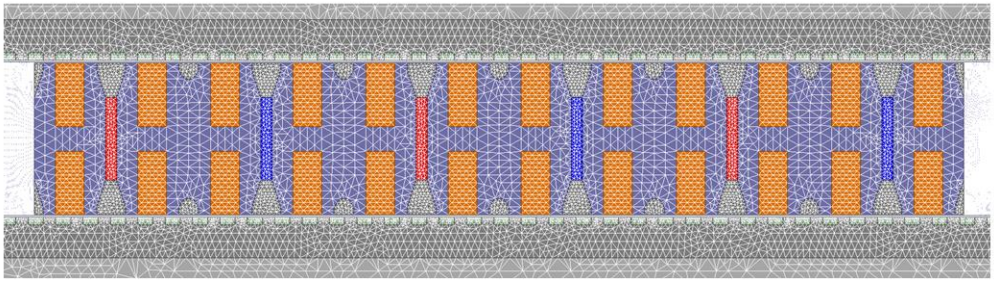

Figure. 2 The mesh division of DLFSPM.

Figure 3 illustrates the back electromotive force (EMF) waveforms of the DLFSPM motor's initial structure under no-load conditions. As depicted in the figure, the waveforms of the three back electromotive forces exhibit a sinusoidal distribution, with an electrical phase shift of 120° between each phase. The waveforms are symmetrical, and the peak values for phases A, B, and C are $E_{ma} = 18.51\text{V}$, $E_{mb} = 20.22\text{V}$, and $E_{mc} = 18.45\text{V}$, respectively. Due to end effects, the amplitude of the back electromotive forces in phases A and C is marginally lower than that in phase B.

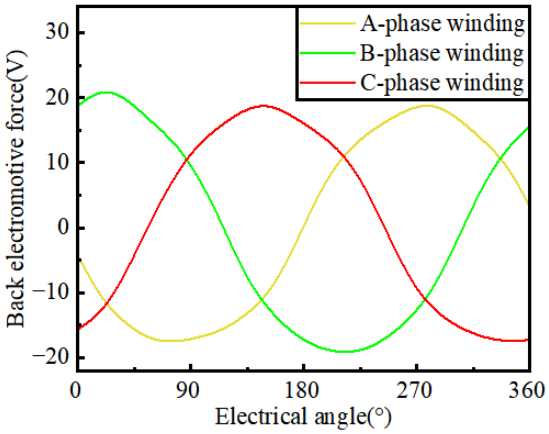

Figure. 3 No-load reverse electromotive force waveforms of DLFSPM.

The presence of harmonics can lead to a degradation in motor performance, increased vibration and noise, and other adverse effects[13]. As illustrated in Figure 4, the harmonic component analysis of the back electromotive force (EMF) in the A-phase winding of the DLFSPM motor reveals that the predominant harmonic components are the third and fifth harmonics, with amplitude ratios relative to the fundamental wave of 7.35% and 2.04%, respectively. The remaining higher-order harmonics have negligible amplitudes and can be disregarded. Consequently, the total harmonic distortion (THD) is determined to be 7.62%.

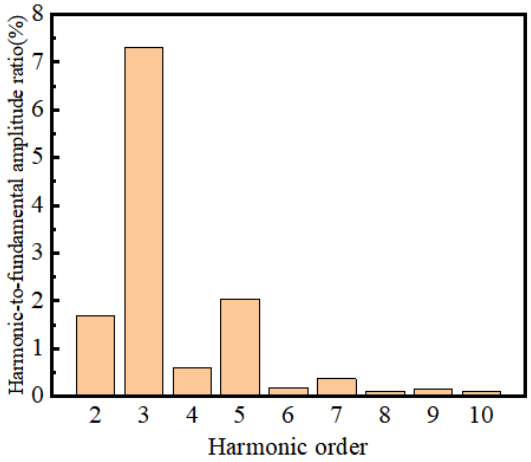

Figure. 4 The harmonic components of the back electromotive force of the A-phase winding.

This study aims to enhance the electromagnetic thrust of the DLFSPM, suppress thrust fluctuations, and minimize electromagnetic vibrations. Therefore, it is essential to identify the factors influencing the electromagnetic thrust prior to optimization. Based on the relationship between power and displacement, and in conjunction with the magnetic co-energy method, the electromagnetic thrust of the DLFSPM motor can be defined as[14]:

$$F_e = \frac{dW}{dx}\bigg|_I = F_r + F_{pm} + F_{cog} \tag{1}$$

Where W represents the work done by the motor thrust, x denotes the displacement of the mover; F_r indicates the magnetic reluctance force of the motor, F_{pm} represents the permanent magnet thrust of the motor, and F_{cog} is the detent force of the motor. The three forces can also be expressed as:

$$F_r = \frac{1}{2} I^T \left(\frac{d}{dx} L\right) I \tag{2}$$

$$F_{pm} = \frac{d}{dx}\left(\psi_{pm}^T I\right) = \frac{3}{2}\frac{2\pi}{\tau_s}\psi_m I_m \cos\alpha = \frac{3\sqrt{2}}{2} \cdot \frac{\pi A_s l_m B_{g\max} l_a c_s k_d k_N \cos_\alpha}{m} \tag{3}$$

$$F_{cog} = -\frac{d\psi}{dx} i = -R_g \phi \frac{d\phi}{dx} = -\frac{1}{2} \phi_m^2 \frac{dR_g}{dx} \tag{4}$$

By integrating the analytical results from Eqs. (2), (3), and (4), the electromagnetic thrust F_e can be determined as follows:

$$F_e = \frac{1}{2} I^T (\frac{d}{dx} L) I + N_{pm} I \frac{d\phi_m}{dx} - \frac{1}{2} \phi_m^2 \frac{dR_g}{dx} \tag{5}$$

Based on the analysis of Eq. (5), the primary factors influencing the electromagnetic thrust of the DLFSPM motor include the armature current I, the dimensions of the motor structure (l_a,l_m), the air-gap magnetic density B_g , and the number of turns per phase winding N_{pm}. Specifically, L denotes the inductance matrix, I represents the armature current matrix, ψ_{pm} signifies the permanent magnet flux matrix, ψ_m is the peak permanent magnet flux linkage, I_m is the peak armature current, α denotes the phase difference between the armature current and the induced electromotive force, R_g represents the air-gap reluctance, ϕ_m is the air-gap flux, τ_s is the secondary pole pitch, and x is the displacement distance of the mover.

Thrust ripple is a critical metric for assessing the operational stability of a motor. It is primarily influenced by the motor's structural dimensions and the air-gap magnetic field. The thrust ripple of the DLFSPM is quantified as a percentage and is expressed by Equation (6) as follows:

$$F_{rip} = \frac{F_{\max} - F_{\min}}{F_{avg}} \times 100\% \tag{6}$$

In the formula, $F_{\max}$, $F_{\min}$, and F_{avg} respectively denote the maximum value, the minimum value, and the average value of the electromagnetic thrust.

Based on finite element analysis, when the rated current $I = 8\text{A}$, the waveform of the electromagnetic thrust of the DLFSPM as a function of the electrical angle is depicted in Figure 5. At this current level, the maximum electromagnetic thrust is 372.31 N, the minimum is 255.28 N, the average thrust is 312.65 N, and the thrust ripple is 37.42%.

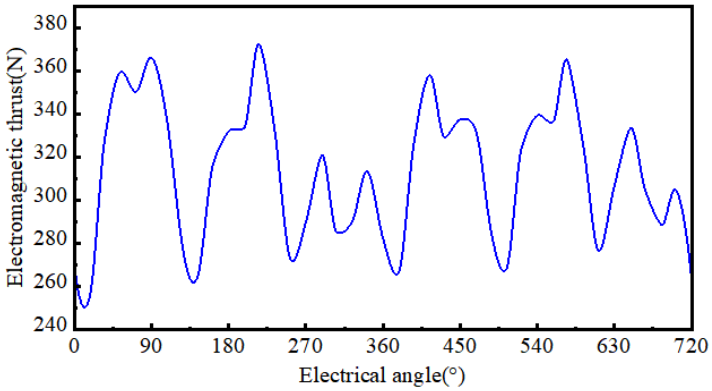

Figure. 5 The Electromagnetic thrust of DLFSPM.

2.3 Electromagnetic vibration characteristics based on the initial structure of DLFSPM

In this study, the stator of the DLFSPM experiences periodic excitation due to electromagnetic forces, leading to vibrational responses. The investigation focuses on the motor's vibrational characteristics across various frequency ranges, including parameters such as stress, displacement, velocity, and acceleration. Analysis of these results can assist in identifying potential resonance risks and areas prone to structural fatigue. Given that the vibration in DLFSPM primarily originate from the two long secondary stators arranged symmetrically, this study simplifies the modal analysis model by conducting modal analysis on a single stator of the initial structure.

The equation of motion describes the dynamic behavior of a system under external excitation[15]. For a linear system, the general form of this equation is:

$$M\ddot{x}(t) + C\dot{x}(t) + Kx(t) = F(t) \tag{7}$$

Where M represents the mass matrix, C denotes the damping matrix, K signifies the stiffness matrix, $x(t)$ is the displacement vector; $\dot{x}(t)$ represents the velocity vector; $\ddot{x}(t)$ is the acceleration vector; and $F(t)$ is the external excitation.

The calculation of stress, displacement, velocity, and acceleration can be performed using the modal superposition method. This method decomposes the system's total response into the contributions from individual modes. Let the modal order be denoted by i, and assume the external excitation $F(t) = F_0 \cos(\omega t)$ is a sinusoidal input. The corresponding response $q_i(t)$, which satisfies Equation (7), can be expressed as:

$$q_i(t) = \frac{F_0}{M_i(\omega^2 - \omega_i^2 + iC_i\omega)} \cos(\omega t) \tag{8}$$

The displacement, velocity and acceleration responses of the system can be calculated by the modal superposition method by superimposing the responses of each mode. It can be expressed as:

$$x(t) = \sum_{i=1}^{n} A_i q_i(t) \tag{9}$$

$$v(t) = \frac{d}{dt} x(t) = \sum_{i=1}^{n} A_i \dot{q}_i(t) \tag{10}$$

$$a(t) = \frac{d}{dt} v(t) = \sum_{i=1}^{n} A_i \ddot{q}_i(t) \tag{11}$$

The calculation of stress is typically performed based on strain, and the expression is given by:

$$\sigma(t) = E\grave{o}(t) \tag{12}$$

In the formula, E represents the elastic modulus of the material, $\grave{o}$ denotes the strain; A indicates the amplitude; ω stands for the angular velocity.

Based on the finite element analysis, the frequency curves of the four vibration response characteristics namely stress, displacement, velocity and acceleration are shown in Figure 6.

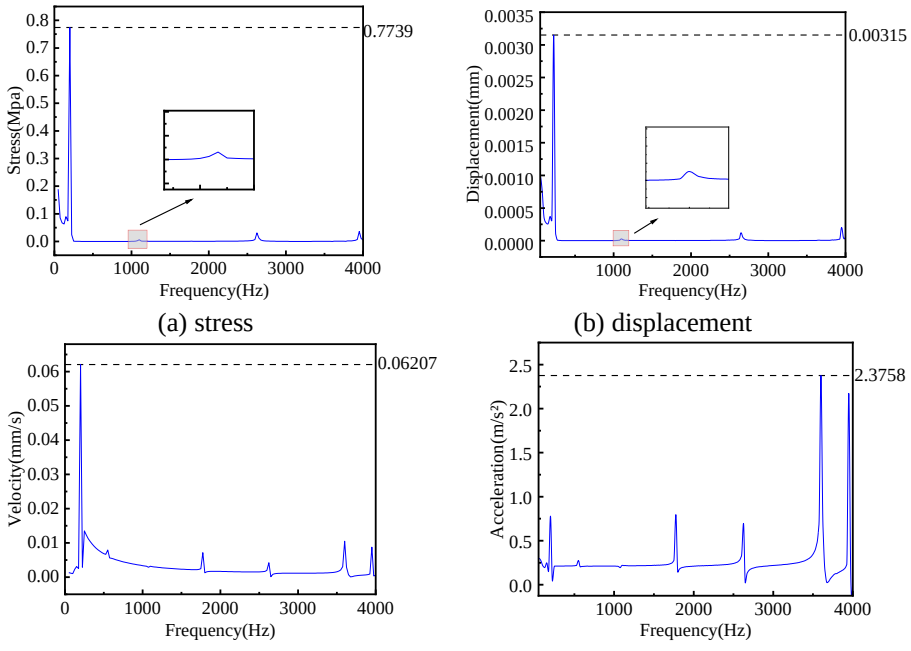

Figure. 6 The Frequency curve diagram of the vibration response for the initial structure of the DLFSPM.

Both stress and displacement reach their maximum values at 200 Hz, with extreme points also occurring at 1100 Hz, 2650 Hz, and 3950 Hz. These four frequencies correspond to the first, third, fifth, and sixth natural frequencies of the stator modes, respectively. According to the electromagnetic force frequency analysis of the DLFSPM, the electromagnetic forces are predominantly concentrated in the low-frequency band. Consequently, the maximum stress and displacement occur at 200 Hz, reaching 0.7739 MPa and 0.0032 mm, respectively. Due to the relatively minor contribution of high-frequency electromagnetic forces, the stress and displacement at other extreme points are comparatively smaller. The variations in stress and displacement exhibit a consistent fluctuation trend with respect to excitation frequency. Physically, displacement is the direct response to the excitation force, while stress arises from the resulting displacement.

The peak values of velocity and acceleration are 0.0621 mm/s and 2.3758 m/s², respectively. The velocity and acceleration curves exhibit extreme points at 200 Hz, 550 Hz, 1750 Hz, 2600 Hz, 3600 Hz, and 3950 Hz, which correspond to the first through sixth natural frequencies of the stator modes. Unlike the displacement and stress responses, although the extreme points for velocity and acceleration occur at the same frequencies, the maximum velocity is observed at 200 Hz, while the maximum acceleration occurs at 3600 Hz. This discrepancy may be attributed to the higher sensitivity of acceleration to frequency variations. Additionally, the extreme values of velocity and acceleration at 3600 Hz and 3950 Hz are significantly larger than those in the lower frequency range. Preliminary analysis suggests that the motor may experience resonance at these two frequencies.

To analyze the above four vibration response characteristics more intuitively, a key frequency of 200 Hz was selected for the cloud chart research. As shown in Figure 7, the cloud charts of the four characteristics at the frequency of 200 Hz are presented.

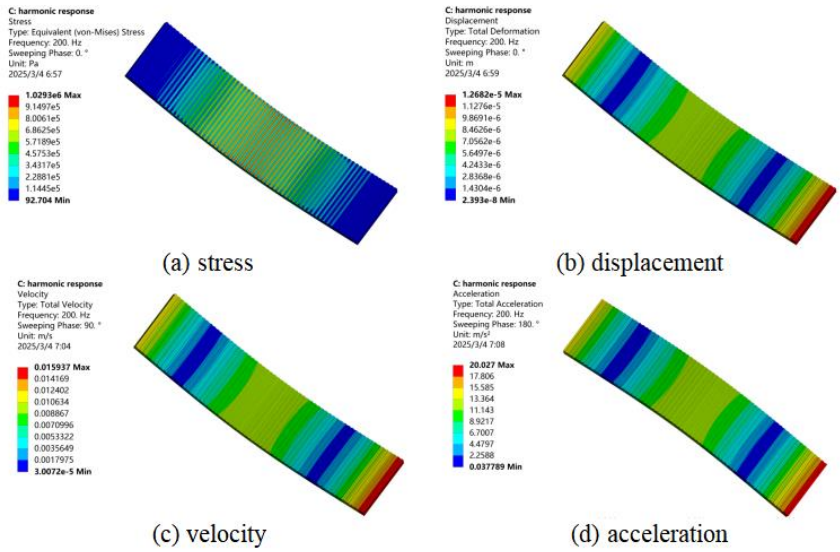

Figure. 7 The Cloud map of stator vibration characteristics for the initial structure of DLFSPM.

From Figure 7(a), it can be observed that the stator of the DLFSPM exhibits relatively high stress in the tooth slots, with a peak value of 1.03 MPa, while the stress at the stator tooth surface is comparatively low. This phenomenon can be attributed to the deep and enclosed nature of the tooth slot region, which increases structural complexity. Consequently, during motor operation, the electromagnetic force exerts a significant effect within the tooth slots, leading to stress concentration in this area. Figures 7(b), 7(c), and 7(d) show that the distributions of displacement, velocity, and acceleration are consistent, with similar response values for the tooth slots and their adjacent tooth surfaces. The response values exhibit a trend of initially increasing from both ends and then decreasing towards the interior, which aligns with the magnetic flux switching process of the DLFSPM motor's stator. At 200 Hz, the maximum values for displacement, velocity, and acceleration are 0.00127 mm, 15.937 mm/s, and 20.027 m/s², respectively.

3. Optimization Design of the Stator Structure for DLFSPM

3.1 The optimization process of the stator structure

According to the analysis in the second part of the paper, the thrust ripple and electromagnetic vibration are mainly influenced by the stator slots and stator teeth structure of the DLFSPM. Therefore, in order to effectively suppress the thrust ripple and electromagnetic vibration, the optimization process of the stator structure is shown in Figure 8. This process describes in detail the process of obtaining a fully optimized stator structure through repeated structural optimization and systematically comparing its performance.

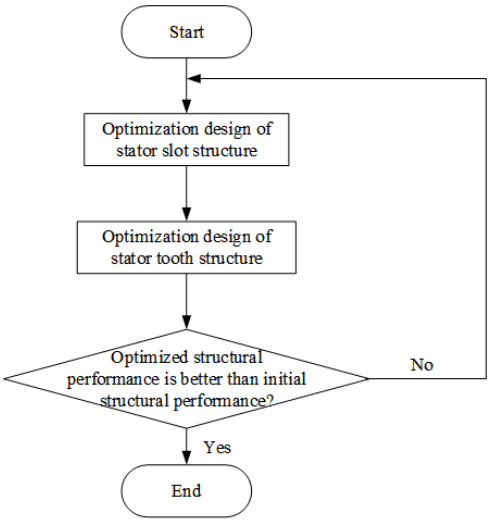

Figure. 8 Flowchart for the optimization design of DLFSPM

3.2 Optimization design of stator slot structure

In the initial design of the DLFSPM, the sharp right-angle slots hinder the smooth flow of magnetic flux lines in this region and result in significant magnetic flux leakage in the stator slots. This phenomenon increases the complexity of the air-gap magnetic flux density harmonics, thereby degrading the motor's output performance. To address this issue, this paper proposes optimizing the internal magnetic field distribution by introducing arc chamfering to the stator slots, which enhances the overall performance of the motor. The arc chamfering scheme is illustrated in Figure 9.

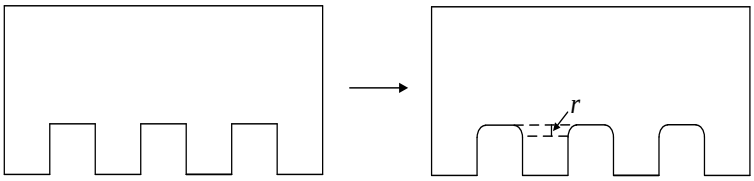

Figure. 9 Schematic diagram of arc chamfering in the stator slot

To investigate the impact of varying stator slot arc chamfer radii on the electromagnetic thrust and thrust ripple in DLFSPM motors, this study sets the arc chamfer radius r within the range of 0.1 mm to 1.5 mm, divided into 15 equally spaced experimental groups (i.e., 0.1 mm, 0.2 mm, ..., up to 1.5 mm). Subsequently, under conditions where the winding current I=8A and the primary mover operates at synchronous speed, simulations are conducted on the DLFSPM. The resulting curves of average electromagnetic thrust and thrust ripple as functions of the chamfer radius are presented in Figure 10.

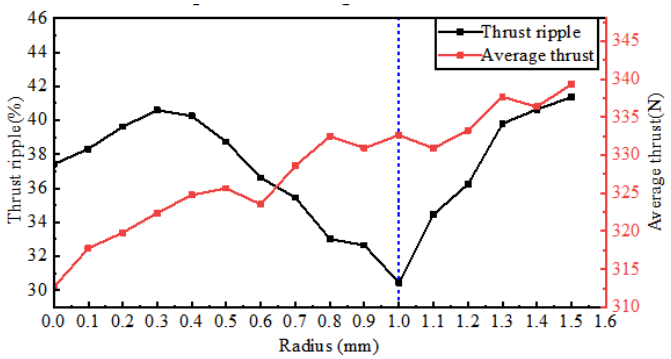

Figure. 10 The curves of the average electromagnetic thrust and thrust fluctuation with the chamfer radius

As illustrated in the figure 10, as the arc fillet radius of the stator slot in the DLFSPM increases, the average electromagnetic thrust exhibits a steadily rising trend. Meanwhile, the thrust ripple initially increases, then decreases, and subsequently rises again. Considering the comprehensive performance of the two key indicators, the optimal chamfer radius

was determined to be 1.0 mm. At this radius, compared with the initial structure, the average electromagnetic thrust increased by 19.99 N, representing a 6.3% increase; the thrust fluctuation decreased by 6.97%, corresponding to an 18.63% reduction.

Figure 11 illustrates the magnetic field line distribution in the stator structure of the DLFSPM after applying a 1.0 mm arc fillet. It is evident that by optimizing the stator design with a 1.0 mm arc fillet radius, the magnetic field lines exhibit significantly reduced leakage and breakage, leading to smoother flux flow in the cogging region, thereby effectively enhancing the overall magnetic field distribution.

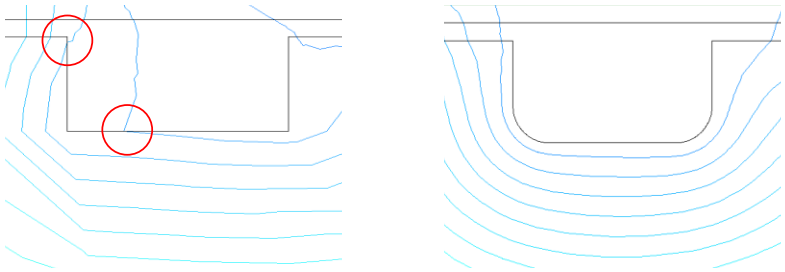

Figure. 11 Comparison of magnetic flux distribution before and after arc fillet optimization of DLFSPM

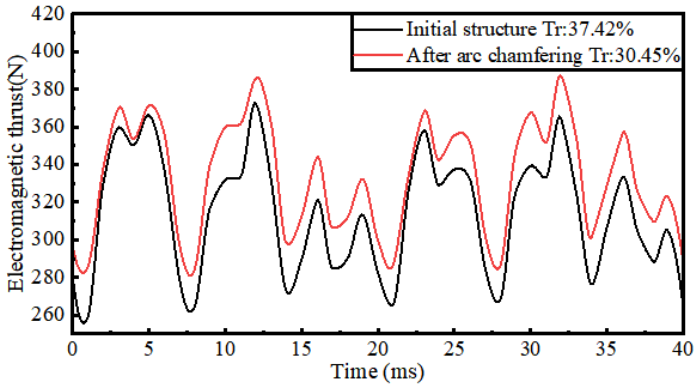

Figure. 12 Comparison of thrust fluctuation before and after arc fillet optimization of DLFSPM

Figure 12 shows the variation curve of the electromagnetic thrust of the DLFSPM after the arc chamfer optimization. It can be seen that compared with the initial structure, the electromagnetic thrust value increases and the fluctuation significantly reduces. The thrust fluctuation drops from 37.42% under the initial structure to 30.45% after the optimization.

3.3 Optimization design of stator tooth structure

In this section, the motor performance is enhanced by introducing rectangular slots on the stator tooth surface. To ensure the effectiveness of this slotting method, it is crucial to first achieve uniform distribution of the auxiliary slots across the stator teeth and secondly, to select appropriate dimensions for the slots, including their depth and width. To determine the optimal rectangular slot dimensions, finite element simulations are conducted using response surface methodology (RSM) and central composite design (CCD). The proposed slotting scheme for the stator tooth surface is illustrated in Figure 13.

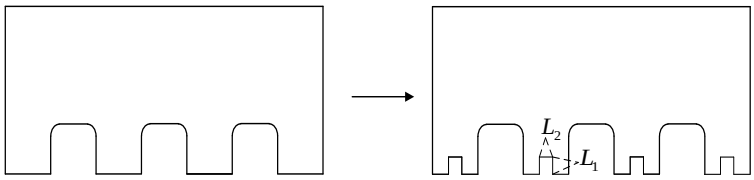

Figure. 13 Schematic illustration of rectangular slots on the stator tooth surface

The RSM is employed to correlate the input design parameters (x_1 , x_2 ,… x_n) with the motor's detent force, electromagnetic thrust and thrust ripple, aiming to identify the optimal dimensions that enhance motor performance. Figure 13 illustrates the variable factors for rectangular slots on the stator tooth surface, where L_1 and L_2 represent the length and width of

the slot, respectively, with dimensions ranging from 0.1 mm to 1.0 mm. By utilizing central composite design, the number of experiments is minimized, and the experimental slot dimensions are set in an arithmetic sequence: 0.1 mm, 0.55 mm, and 1.0 mm.

L_1 and L_2 correspond to the independent factor code values x_1 and x_2 in the optimization function. The quadratic polynomial relationship between the two independent factors x_1 and x_2 and the target response function Y can be expressed as:

$$Y = \alpha_0 + \sum_{i=1}^{n} \alpha_i x_i + \sum_{i=2}^{n} \alpha_{ii} x_i^2 + \sum_{i=1}^{n} \cdot \sum_{j=1}^{n} \alpha_{ij} x_i x_j \quad (i < j) \tag{13}$$

The objective function Y_1 is defined as the percentage of the peak detent force relative to the average electromagnetic thrust, while the objective function Y_2 represents the thrust ripple. The total objective function Y is a weighted sum of Y_1 and Y_2, each contributing 50%. The finite element simulation results are presented in Table 2.

Table 2 Finite element simulation results of stator tooth surface grooving

Number of experiments	L_1/mm	L_2/mm	Y_1	Y_2
1	0.1	0.1	18.59	27.78
2	1.0	0.1	16.58	29.88
3	0.1	1.0	18.92	28.74
4	1.0	1.0	19.19	30.71
5	0.1	0.55	17.35	27.14
6	1.0	0.55	16.44	26.21
7	0.55	0.1	18.21	25.98
8	0.5	1.0	17.21	27.83
9	0.55	0.55	15.77	26.47

The regression equation of the objective function, derived from the experimental data, is as follows:

$$Y = 24.949 - 7.2437x_1 - 9.1394x_2 + 1.3272x_1x_2 + 6.0041x_1^2 + 8.5844x_2^2 \tag{14}$$

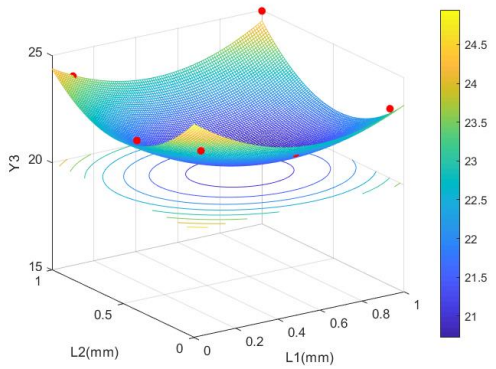

Figure. 14 The three-dimensional response surface plot of the objective function

The three-dimensional response surface plot of the objective function is presented in Figure 14. As illustrated in the figure.14, when L_1=0.55mm and L_2=0.49 mm, the objective function Y attains its minimum value of 20.723. Compared to the results following the optimization of the stator slot arc chamfering, further optimization using stator tooth surface technology resulted in an increase of 15.61 N in the average electromagnetic thrust of the DLFSPM, corresponding to a 4.7% increase; the thrust ripple decreased by 4.26%, representing a reduction of 13.99%. The performance comparison of the DLFSPM motor's initial structure, after stator slot arc chamfering treatment, and after stator tooth rectangular slotting is presented in Table 3 and Figure 15.

Table 3 Comparison of motor performance before initial structure, after arc chamfering treatment and after rectangular slotting

Structure of DLFSPM	Average electromagnetic thrust	Thrust ripple
initial structure	312.65 N	37.42%

after stator slot arc chamfering treatment	332.63 N	30.45%
after stator tooth rectangular slotting	348.24 N	26.16%

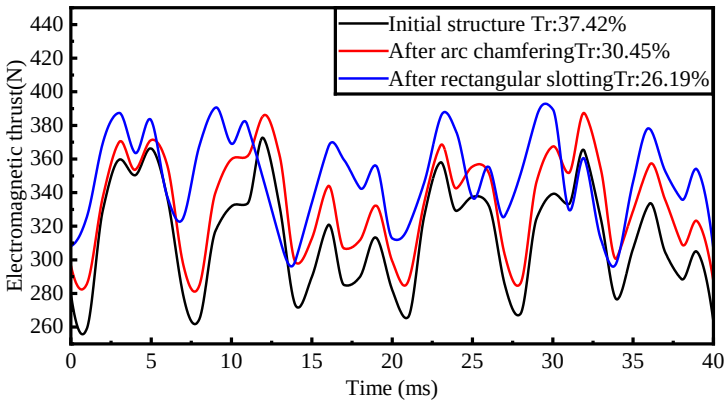

Figure. 15 Comparison of motor performance before initial structure, after arc chamfering treatment and after rectangular slotting

3.4 Comparison of electromagnetic vibration performance before and after optimized structure

Through the aforementioned stator structure optimization, it is evident that the performance of the DLFSPM motor has been significantly enhanced. Compared to the initial design, the optimized motor exhibits higher electromagnetic thrust and reduced thrust ripple. The initial structure and the fully optimized stator configuration of the DLFSPM topology are illustrated in Figure 16.

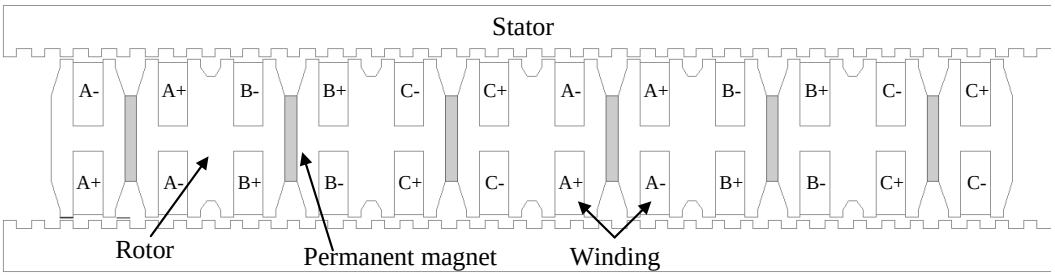

(a) Initial structure of the DLFSPM

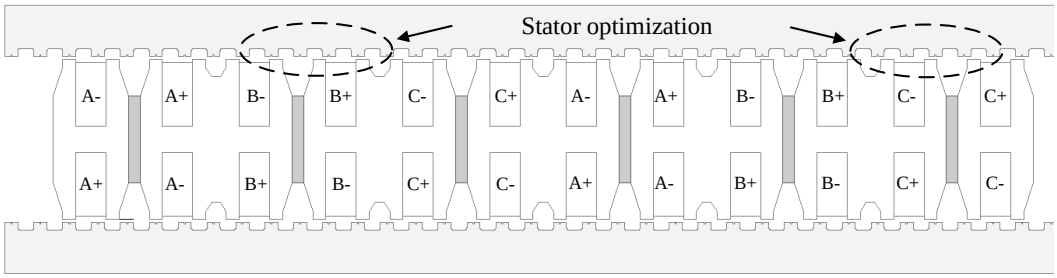

(b) Optimized structure of the DLFSPM

Figure. 16 Comparison between initial structure, and optimized structure of the DLFSPM

In this section, a detailed comparative analysis of the electromagnetic vibration characteristics of the DLFSPM before and after optimization is presented. Figure 17 presents a comparative analysis of the total harmonic distortion (THD) rates of the DLFSPM before and after structural optimization. The results show that the back electromotive force (EMF) of the initial structure contains a significant number of harmonic components, resulting in a THD of 7.62%, primarily composed of odd harmonics such as the 3rd and 5th. Following optimization, the THD is reduced to 5.35%, indicating a substantial suppression effect.

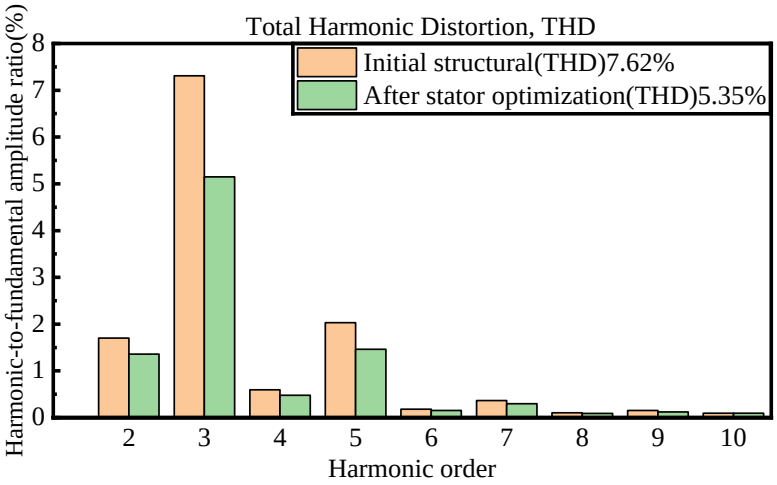

Figure. 17 Comparison of total harmonic distortion (THD) before and after optimization of DLFSPM

The electromagnetic harmonic force generated by the optimized DLFSPM is used as the excitation load for a simulation analysis of the motor's electromagnetic vibration characteristics. The analysis yielded frequency response curves and cloud maps for four key indicators: stress, displacement, velocity, and acceleration. These results are presented in Figures 18 and 19.

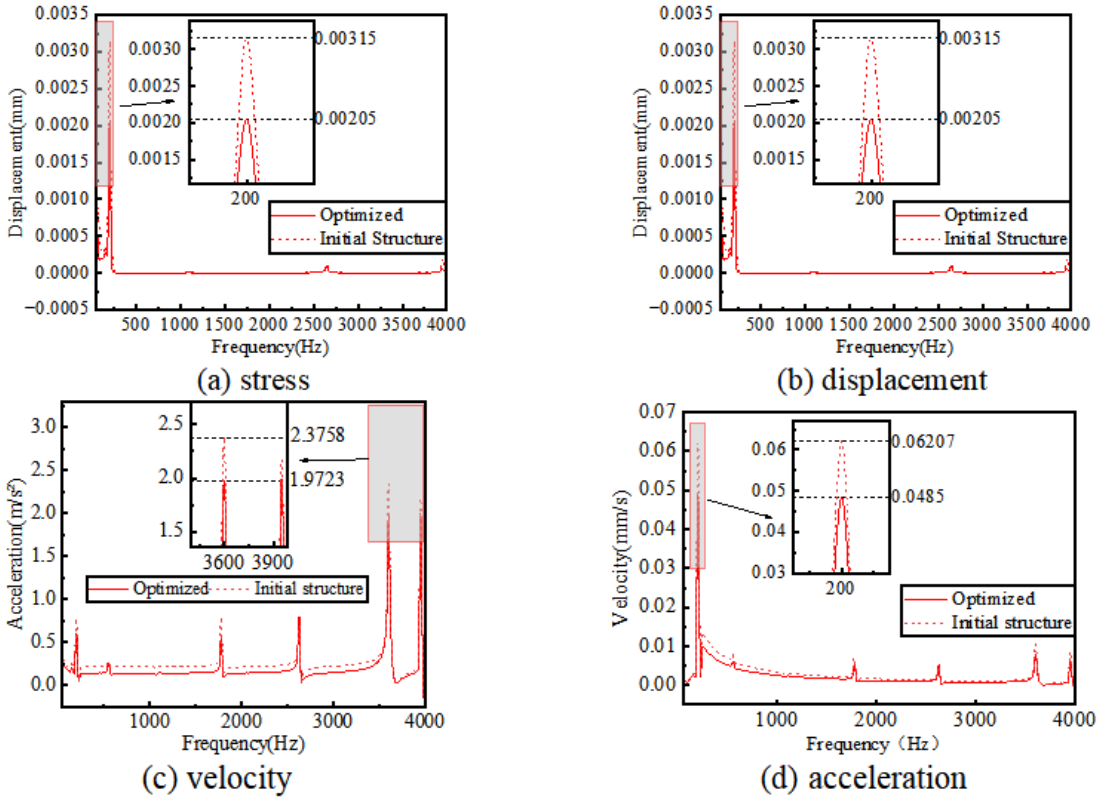

Figure. 18 Comparison of frequency curve diagram of the vibration response before and after optimization of DLFSPM

As shown in Figure 18, compared with the initial structure, the maximum stress frequency response of the motor stator decreased from 0.7739 MPa to 0.5718 MPa, representing a reduction of 26.11%; the maximum displacement frequency response decreased from 0.0032 mm to 0.0021 mm, a reduction of 34.38%; the maximum velocity frequency response decreased from 0.0612 mm/s to 0.0485 mm/s, a reduction of 20.75%; and the maximum acceleration frequency response decreased from 2.3758 m/s² to 1.9723 m/s², a reduction of 16.98%. The overall reduction in these vibration frequency response values indicates that the harmonic distortion rate of the motor's electromagnetic force has been effectively mitigated.

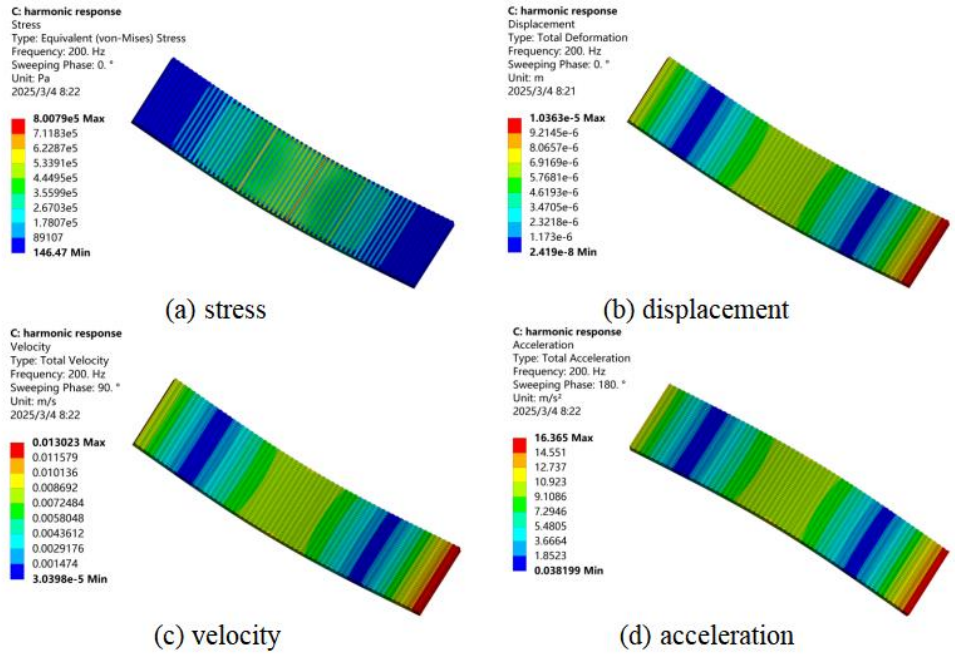

Figure. 19 The Cloud map of stator vibration characteristics for the optimized structure of DLFSPM.

As shown in the figure 19 and figure 7, compared with the initial structure, the maximum stress response of the motor stator decreased from 1.0293 MPa to 0.8008 MPa, representing a reduction of 22.2%; the maximum displacement response decreased from 0.01268 mm to 0.01036 mm, a reduction of 18.3%; the maximum velocity response decreased from 15.94 mm/s to 13.023 mm/s, a reduction of 18.3%; and the maximum acceleration response decreased from 20.027 m/s² to 16.365 m/s², a reduction of 18.29%. The significant reductions in these four vibration responses indicate that the system's vibration amplitude has diminished, and the load it bears has been alleviated, thereby reducing the risk of fatigue, fracture, or deformation of the stator. These results verify that the optimized structure effectively mitigates the electromagnetic vibration of the DLFSPM motor.

4. Conclusion

This paper achieves the goal of enhancing the electromagnetic thrust output of the DLFSPM, suppressing thrust fluctuations and electromagnetic vibrations by conducting a comprehensive optimization of the stator structure. The following conclusions can be drawn from this study.

The relationship between the arc chamfer radius of the stator slot and the electromagnetic thrust as well as thrust ripple in the DLFSPM motor is investigated, and an optimal chamfer radius of 1 mm is determined, thereby optimizing the stator slot structure. The dimensions of the rectangular auxiliary slot are optimized through finite element simulation experiments employing Response Surface Methodology (RSM) and Central Composite Design (CCD), thereby enhancing the stator tooth structure. Based on finite element analysis, a comparative study is conducted between the initial and optimized structures of the DLFSPM. The simulation results demonstrate that after optimization, the electromagnetic thrust increased by 11.5%, the thrust ripple decreased by 11.3%, and all four key indicators of electromagnetic vibration are reduced by more than 16%.This comprehensive optimization method effectively suppresses the thrust ripple and electromagnetic vibration in the DLFSPM motor, significantly improving the stability and output performance of its operation.

Declaration of Conflicting Interests

The author(s) declared no potential conflicts of interest with respect to the research, author-ship, and/or publication of this article.

Data Sharing Agreement

The datasets used and/or analyzed during the current study are available from the corresponding author on reasonable request.

Acknowledgements

This work was Funded by Science and Technology Project of Hebei Education Department under Grant QN2020155.

References

[1] Wen C., Zhao Q., Li M., Liu J., Li M., and Zhao X. (2022) Multi-objective Optimization Based on Hyperparameter Random Forest Regression for Linear Motor Design, International Journal of Machine Learning and Cybernetics, 13(10): 2929-2942.

[2] Shahid H., Faisal K., Wasiq U., Basharat U. and Bakhtiar K. (2021) Development of a Low-Cost Modular Structure Fault Tolerant Field Excited Flux Switching Linear Machine for Urban Rail Transit, IEEE ACCESS, 9: 165854-165864.

[3] Yuxiao Z., Yongkuan L., Yujian C., Jiaming L. and Jin, C. (2024) Comparative Analysis of Normal Force Characteristics and Dynamic Influence of Linear Flux-switching Permanent Magnet Motor for Rail Transit, IEEE ACCESS, 12: 132409-132420.

[4] Liu Y., X. Huang, J. Li, and W. Yu. (2023) Magnetic field analysis and thrust optimization of ARC permanent magnet synchronous motor combined with linear mover and ARC stator, IEEE Transactions on Industry Applications, 59(5): 5867-5874.

[5] Xingfa S., Jin X., Junjie Z., and Wei X. (2023) Thrust Ripple Suppression Based on Negative Current Control for Short-Primary Low-Speed Large LIM under Transient Operation, IEEE Transactions on Energy Conversion, 38(3): 1566-1575.

[6] Zhao M., Kong Z., Tang P., Zhang Z., Yu G., Zhang H., Xu Y., and Zou, J. (2023). Design and Optimization of Linear Permanent Magnet Vernier Generator for Direct Drive Wave Energy Converter. Energies, 16(7), 3164

[7] M. Cheng, B. Zhang, S. Wang, and W. Wang. (2021) Modular thin yoke linear flux-switching permanent magnet machine and control system, Journal of Electrical Engineering, 16(1)1: 1–8.

[8] M. Cheng, P. Han, Y. Du, H. Wen, and X. Li. (2022) A tutorial on general air-gap field modulation theory for electrical machines, IEEE Journal of Emerging and Selected Topics in Power Electronics, 10(2):1712–1732.

[9] P. Wang, W. Hua, G. Zhang, B. Wang, and M. Cheng. (2022) Principle of flux-switching permanent magnet machine by magnetic field modulation theory Part I: Back-electromotive-force generation, IEEE Transac-tions on Industrial Electronics, 69(3): 2370-2379.

[10]P. Wang, W. Hua, G. Zhang, B. Wang, and M. Cheng. (2022) Principle of flux-switching permanent magnet machine by magnetic field modulation theory Part II: Electromagnetic Torque Generation, IEEE Transac-tions on Industrial Electronics, 69(3): 2437-2446.

[11]Arslan, S. (2024) Developing a Tubular Type Flux-Switching Permanent Magnet Linear Machine for a Semi-active Suspension Systems, International Journal of Automotive Technology, 25: 1201–1214.

[12]Y. Zhou, C. Shi, R. Qu, D. Li, and Y. Gao, (2021) Overview of flux modulation linear permanent magnet machines, Proceedings of the CSEE, 44(4):1469-1484.

[13]Nie L. and J. Fang.(2024) Optimization of coreless high temperature superconducting linear synchronous motor, IEEE Transactions on Applied Superconductivity, 34(8): 3603704.

[14]Ji, J., X. Zhu, H. Tang, L. Xu, and W. Zhao, (2023) Design to improve thrust force performance of dual-side primary permanent-magnet vernier linear motor, Chinese Journal of Electrical Engineering, 9(2): 1-13.

[15] Xiaoyong Z., Jiamin B., Zixuan X. Yunyun, C. and Li, Q. (2025) Low-Vibration Design and Investigation of a Consequent-Pole PM Motor Utilizing Composite MMF and Subarea Permeance, IEEE Transactions on Transportation Electrification, 11(1): 3568-3579.